GDCh Research Article Angewandte International Edition Chemie www.angewandte.org

How to cite: *Angew. Chem. Int. Ed.* **2025**, e202505232
doi.org/10.1002/anie.202505232

Solid State Batteries

Adaptive 3D Cross-Linked Single-Ion Conducting Polymer Electrolytes Enable Powerful Interface for Solid State Batteries

*Zhaoxia Yang, Yuning Ye, Nan Meng, and Fang Lian**

Abstract: Single-ion conducting polymer electrolytes (SICPEs) are designed by covalently bonding anions to the polymers, which is attractive for mitigating anion aggregation-derived polarization. However, one major challenge for developing SICPEs with higher ambient ionic conductivity comes at the expense of structural robustness. Here, boron ion-centered lithium salt (LiT4PAB) with symmetric cross structure and terminal functional C=C was proposed as a units, and then 3D coordination electrolyte (LiPHB) was constructed via chemical cross-linking of LiT4PAB with poly(vinylidene fluoride-co-hexafluoropropylene) (PVDF-HFP). The boron ion-centered units catenated by single bonds show the abundant conformation transitions, enabling the deformable architecture of LiPHB with the aid of electrostatic interactions of diphenylsulfonimide. Therefore, LiPHB undergoes adaptive deformation when subjected to impact, achieving good ductility with elastic moduli of 1.4 GPa and a maximum elongation of 447.4%. Moreover, LiPHB demonstrates 3D single lithium-ion transport channels to guide the homogeneous lithium deposition. As a results, lithium symmetric cells exhibit stable plating/stripping cycle for over 1500 h at 0.1 mA cm^{-2} at 30 °C. Li/LiPHB SICPEs/NCM811 solid-state batteries deliver a capacity retention of 90.3% in 150 cycles at 30 °C and 0.2 C. Our study shed light on the design strategies of the dynamic single-ion conducting polymer electrolytes for solid-state batteries.

Introduction

Solid polymer electrolytes (SPEs) have the particular advantages of high flexibility, strong adhesion, good processability, and excellent interfacial compatibility.[1–3] Moreover, it is important to find by Chazalviel that anion migration under the electric field is the primary factor creating the space charge region in the vicinity of the metal deposition side, accelerating the growth of lithium dendrites.[4–6] The concept of single lithium-ion conductor was proposed by Bannister et al. in the early 1980s.[7] Unlike the "salt-in-polymer" SPEs prepared by dissolving a lithium salt in a polymer host such as PEO-based electrolytes, single lithium ion conducting polymer electrolytes (SICPEs) are designed by covalently bonding anions to the polymers (named as polyanions[8]), enabling high transference number of cations (t_{Li}^+).[9–11] Therefore, SICPEs with intrinsically high t_{Li}^+ possess numerous virtues, including mitigating the ion concentration gradient and derived problems, suppressing the growth of lithium dendrites, improving the utilization of cathode materials, and promoting the rate performance of solid-state batteries (SSBs).[12–14] However, SICPEs appear to have low ionic conductivity (10^{-7}–10^{-5} S cm^{-1}) at room temperature due to the abundant rigid groups, high glass transition temperature (T_g), and constrained mobility of the polymer segments.[15–17] In recent studies, how to further improve the ambient lithium-ion conductivity of SICPEs without compromising of natural rigidity and mechanical strength has been a big challenge.[18,19] One of the best solutions to the above-mentioned problem is to construct the robust cross-linked polymers with stimuli-responsive deformation capability, in which rotation and extension of bond occur rather than dissociation or break.[20,21]

Liu team developed a boron-PDMS transient cross-linked polymer with solid-liquid hybrid behavior arising from the dynamic covalent bonds, serving as a dynamic interfacial layer for lithium metal anodes.[22] Ye et al. fabricated a self-healing polyurethane (PNPU) via one-pot polycondensation, where hydrogen-bond cross-linking enables reversible network reconfiguration under mechanical stress and enhanced interfacial stability of the solid-state polymer electrolyte.[23] Zhao et al. adopted a mechanically interlocked network (MIN) based on sliding alkene-functionalized [2]rotaxane, demonstrating energy dissipation and cyclic volume tolerance during high-capacity Li deposition/stripping.[24] The inherent structural instability may lead to mechanical degradation during long-term cycling. In comparison with dynamic physical interaction, a static cross-linking framework catenated by stable covalent bonds ensures superior mechanical integrity.[25–27] Du et al. developed a novel ionic covalent organic framework material (ICOF) based on a spiroborate skeleton,[28] which endowed the material with excellent thermal stability and ionic conductivity of 3.05×10^{-5} S cm^{-1} at room temperature. But incorporating rigid group, such as benzene rings,[27–29] imidazole rings,[30] polyimides,[31] and nitrile polymers,[32] into polymerization processes inherently restricts the rotational flexibility of bonds. Therefore, it is

[*] Dr. Z. Yang, Dr. Y. Ye, Dr. N. Meng, Prof. F. Lian
School of Materials Science and Engineering, University of Science and Technology Beijing, Beijing 100083, P.R. China
E-mail: lianfang@mater.ustb.edu.cn

Additional supporting information can be found online in the Supporting Information section

crucial to strategically integrate the advantages of rigidity and deformability in structural design.

Herein, novel boron ion-centered lithium salt LiT4PAB with a symmetric cross structure was proposed as units and followed by 3D chemical cross-linking with the poly(vinylidene fluoride-co-hexafluoropropylene) (PVDF-HFP) to achieve robust-adaptive framework LiPHB SICPEs. LiT4PAB catenated with single bonds shows the abundant transitions of conformation. As well as accerlating under the electrostatic interactions with diphenylsulfonimide (BBI), 3D-architechitured LiPHB undergoes adaptive deformation when subjected to impact, dissipating energy to achieve good mechanical ductility with a tensile strength of 2.35 MPa, elastic moduli of 1.4 GPa, and a maximum elongation of 447.4%. It shows not only high lithium-ion transference number ($t_{Li}{}^{+} = 0.7$) and ionic conductivity of 5.9×10^{-4} S cm^{-1} at 30 °C but also good thermal stability up to 358.3 °C and a wide electrochemical stability window (4.6 V in NCM811 batteries). Furthermore, the abundant fluorine in PVDF-HFP contributes to LiF-rich solid electrolyte interphase (SEI) layer during the cycling process.[23,33] As a result, lithium–lithium symmetric cells exhibit stable cycling for over 1500 h at 0.1 mA cm^{-2} and for 200 h at 0.2 mA cm^{-2} with critical current density (CCD) up to 1 mA cm^{-2}. Importantly, even under stringent conditions, the nucleation overpotential of the initial Li deposition on Cu foil is only 26.5 mV with a Coulombic efficiency of 87.1%, revealing the mechano-electrochemical coupling interface stability of LiPHB SICPEs. Meanwhile, the Li/LiPHB SICPEs/NCM811 solid-state batteries demonstrate a reversible capacity of 140 mAh g^{-1} with a capacity retention rate of 90.3% over 150 cycles at 30 °C and current density of 0.2 C. Boron-based SICPEs can accommodate significant volume changes during battery cycling and exhibit exceptional electrochemical stability. This work provides a new paradigm to develop 3D-architected adaptive SICPEs for high-energy-density solid-state batteries.

Results and Discussion

Structure and Morphologies

The constructing principle of lithium tetra-(4-pentenoic acid) borate (LiT4PAB) and the single-ion conducting polymer electrolyte LiT4PAB-PVDF-HFP-BBI (LiPHB) are presented in Figure 1, with detailed reaction mechanisms available in the Supporting Information. Typically, LiT4PAB is synthesized through a one-pot reaction, while LiPHB is fabricated via a solution-processable method (Figure S1). Figure S2 displays the nuclear magnetic resonance (NMR) patterns of LiT4PAB. In the ^{1}H spectrum (Figure S2a), the chemical shifts at 5.8, 4.9, and 4.8 ppm are assigned to the —CH=CH$_2$ group, while the ones at 2.2 and 2.0 ppm can be attributed to the —CH$_2$—CH$_2$— groups, which are on the ligands of —COO—. Moreover, the ^{13}C NMR spectrum of Figure S2b displays that the septet at a chemical shift of 39.8 ppm corresponds to the deuterated DMSO solvent peak. And the chemical shift at 177.6 ppm is identified to be the characteristic signals of the —COO— group; the ones at 139.7

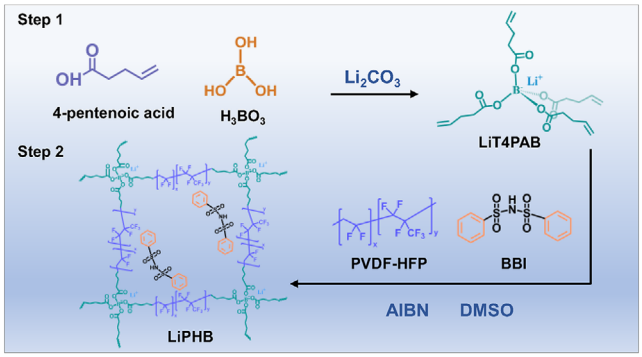

Figure 1. Schematics for construction principle of LiT4PAB and LiPHB SICPEs.

and 114.3 ppm are assigned to the —CH=CH$_2$ group; and the ones at 37.1 and 30.5 ppm can be attributed to the —CH$_2$—CH$_2$— groups, which are on the ligands of —COO—. In the ^{11}B NMR spectrum of Figure S2c, the characteristic peak at 11.6 ppm belongs to the BO_4^- group, and the peak at 0.7 belongs to the borosilicate nuclear magnetic tube. Apart from the solvent peak, there are almost no impurity peaks in NMR spectrum, indicating the high purity of the LiT4PAB samples. Moreover, in Fourier-transform infrared spectroscopy (FT-IR) spectrogram (Figure S3), the characteristic peaks of —OH (3000 cm^{-1}) and C=O (1712 cm^{-1}) for carboxyl group characteristic peaks in 4-pentenoic acid disappear, indicating a complete esterification. Additionally, the peaks at 1575 and 1556 cm^{-1} of LiT4PAB correspond to C=C group, while the peaks at 1436 and 1415 cm^{-1} are identified as the stretching vibration of carboxylate C—O bonds. Simultaneously a characteristic peak of B—O appears at 1333 cm^{-1}. Therefore, LiT4PAB with symmetric cross structure was determined by NMR and FT-IR. In addition, Figure S4 illustrates the HOMO and LUMO energy levels of LiBOB, LiODFB, $LiBF_4$, and LiT4PAB. In comparison with the other boron-based lithium salts, LiT4PAB demonstrates superior oxidative and reductive stability in terms of LUMO (−4.207 eV) and HOMO (−9.946 eV) values. Especially, a smaller HOMO–LUMO gap (ΔE = 5.739 eV) implies a closer electron energy distribution, suggesting that LiT4PAB with an enhanced reactivity is suitable as unit for further polymerization.[34]

Figure S5 comparatively displays the XRD patterns of LiT4PAB, BBI, PVDF-HFP, and LiPHB. The peak at 20.5° corresponds to the (110) plane of α-phase PVDF-HFP.[35] Obviously, the characteristic peaks of LiT4PAB and BBI are not detectable in the LiPHB sample due to their complete incorporation. The FT-IR spectra in Figure S6 demonstrate that the C=C characteristic peaks of vibration at 1575 and 1556 cm^{-1} originate from LiT4PAB, which are undetectable in LiPHB. Moreover, the S=O characteristic vibration peaks at 1045 cm^{-1} are not detectable in LiPHB, indicating the absence of trace DMSO in the membrane. The peaks at 1166 cm^{-1} correspond to the symmetric stretching mode of —CF$_2$— in PVDF-HFP, while the peaks at 837 and 872 cm^{-1} are identified as the amorphous regions of PVDF-HFP.[36] This indicates a cross-linking reaction between the LiT4PAB

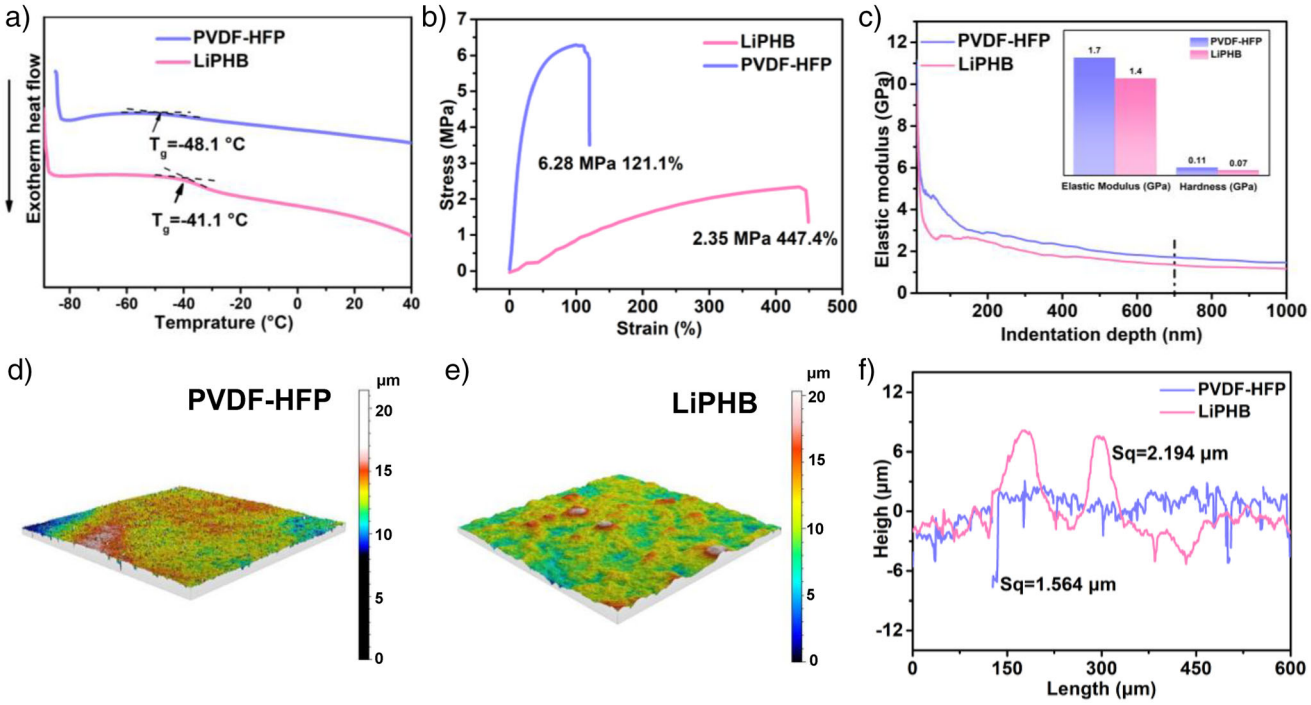

Figure 2. a) DSC of PVDF-HFP and LiPHB; b) Stress–strain curves of LiPHB and LiPH; c) Elastic modulus–distance loading curves of PVDF-HFP and LiPHB (inset is a contrast bar graph of the elastic modulus and hardness of PVDF-HFP and LiPHB). d)–f) The roughness of PVDF-HFP and LiPHB.

and PVDF-HFP. Besides, the N─H signal at 3472 cm^{-1} and the characteristic peaks of the benzene ring appear in LiPHB, which suggests that BBI has not participated in the cross-linking reaction. Additionally, the C─SO_2─N and benzene ring characteristic peaks show a slight blue shift from 1360 cm^{-1} (BBI) to 1400 cm^{-1} (LiPHB), which is possibly due to the weak electrostatic interaction between BBI and the polymer matrix.

The morphology of the LiT4PAB powder is shown in Figure S7a, while Figure S7b demonstrates that the PVDF-HFP membrane is uniformly flat with evenly distributed pores. Figure S7c–e shows the surface and cross-section image of the membrane of the LiPHB SICPEs, illustrating the uniform morphology. In Figure S7f–i, the mapping spectrum of the O, F, and S elements indicates a uniform distribution of LiT4PAB, PVDF-HFP, and BBI in the skeleton. Thermogravimetry (TGA) results (Figure S8) show that the onset decomposition temperatures are 428.9 °C for LiT4PAB, 415.6 °C for PVDF-HFP, and 358.3 °C for LiPHB, indicating good thermal stability of the LiPHB polymer membrane. To further validate its thermal stability, the membrane was kept at different temperatures for 10 min, and its deformation was recorded. As shown in Figure S9, it is evident that the electrolyte membrane exhibits good thermal stability up to 120 °C and a slight shrinkage even at 180 °C.

Mechanical Properties and Configuration Calculations

In addition to thermal stability, the architectured structure affects the mechanical flexibility of the electrolyte membrane. Differential scanning calorimetry DSC test results (Figure 2a) indicate that the glass transition temperatures of PVDF-HFP and LiPHB are −48.1 and −41.1 °C, respectively, suggesting excellent segmental mobility of LiPHB. Additionally, after cross-linking PVDF-HFP with LiT4PAB, the ultimate elongation increased from 121.1% to 447.4%, and the mechanical strength is 2.35 MPa (Figure 2b), indicating that LiPHB has strong elastic deformation capability. Additionally, the stress–strain curves of LiPH (the same as LiPHB preparation except that no BBI is added) and LiPHB with PC in Figure S10 demonstrate their ultimate elongations are 437.2% and 466.4%, respectively, indicating that the mechanical properties of the electrolyte membranes were little affected by the introduction of BBI and trace PC. Furthermore, as observed from the nanoindentation test in Figure 2c, the elastic moduli for PVDF-HFP and LiPHB are 1.7 and 1.4 GPa, while the hardness is 0.11 and 0.07 GPa, respectively, indicating that LiPHB possesses a greater capacity for reversible deformation within the elastic range, especially ductility, when subjected to impact or deformation.[37] The surface roughness of PVDF-HFP and LiPHB was assessed via laser scanning confocal microscopy (LSCM) (Figure 2d–f). The root mean square roughness (Sq) of LiPHB is marginally higher than that of PVDF-HFP, and the 3D rendering graphs reveal a more architectured surface of LiPHB, which is in agreement with the SEM characterization results. This indicates that the cross-linking process converts the linear polymer chains into a three-dimensional network, thereby achieving the distinct mechanical properties.

To further analyze the dynamic structural characteristics of net rack configuration, the bond angles of the optimized

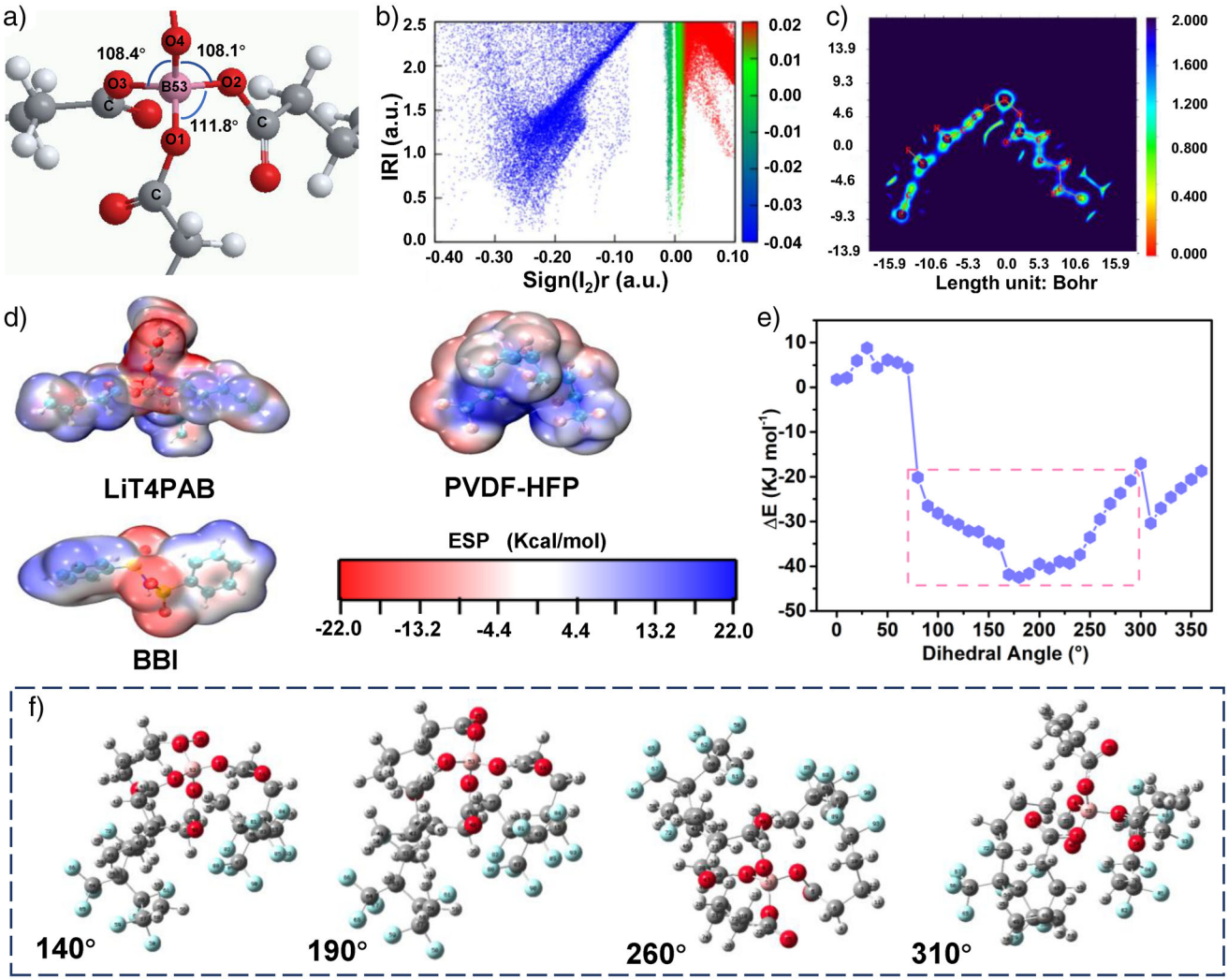

Figure 3. a) The bond angles of LiT4PAB; b) The IRI scatter plot and c) the IRI planar color map of LiPHB; d) Molecular electrostatic potential of LiT4PAB, BBI, and PVDF-HFP e) and f) Various stable conformations of the cross-linking site structure with the dihedral angle O3-B53-O2-C5 rotating from 0° to 360° at low system energy.

structure were examined. As shown in Figure 3a, the O—B—O bond angles at 108.1°, 108.4°, and 111.8° are detectable for a B sp^3 tetrahedral configuration, indicating the role of boron-based lithium salt LiT4PAB as a cross-linking point of 3D network. Moreover, the weak interaction plot (Figure S11), the interaction region indicator (IRI) scatter plot (Figure 3b), and the IRI planar color map (Figure 3c)[38] visually reveal the uniformly distributed weak interactions along LiPHB. The blue regions indicate chemical bonding, and the red regions indicate steric hindrance. Moreover, the green regions represent weak van der Waals interactions and halogen bonding attractions. Therefore, the uniform distribution of weak interactions and the flexible bond angle of LiT4PAB as the cross-linking site contribute to the dynamic conformation of LiPHB. The electrostatic potential energy was calculated by density functional theory (DFT).[39] In Figure 3d, the sulfonyl imide group in BBI and the C—F bond electrostatic region in PVDF-HFP are negative with marked as red regions, showing a certain nucleophilic ability to adsorb lithium ions, which is consistent with the analysis results of the existing weak interaction as described above. Simultaneously, BBI demonstrates a blue shift of the peaks in FT-IR, corroborating its interaction with the polymer matrix.

The flexibility of LiPHB segments mainly depends on the ability of the segments to change their conformation through rotation around the main chain. Figure 3e shows the energy variation of the system with the rotation of the dihedral angle. The energy difference between two stable conformations is identified with Δutg. For example, Δutg = 2.7 KJ mol^{-1} for the conformations at 140° and 260° indicates excellent equilibrium flexibility. Moreover, the maximum energy barrier Δub to overcome between the two stable conformations is only 12.1 KJ mol^{-1}, demonstrating its good dynamic deformability. Furthermore, Figure 3f illustrates several stable conformations of the cross-linking site structure as the dihedral angle O3-B53-O2-C5 rotates from 0° to 360° with low energy barrier. Evidently, the abundant conformations indicate that the boron-centered

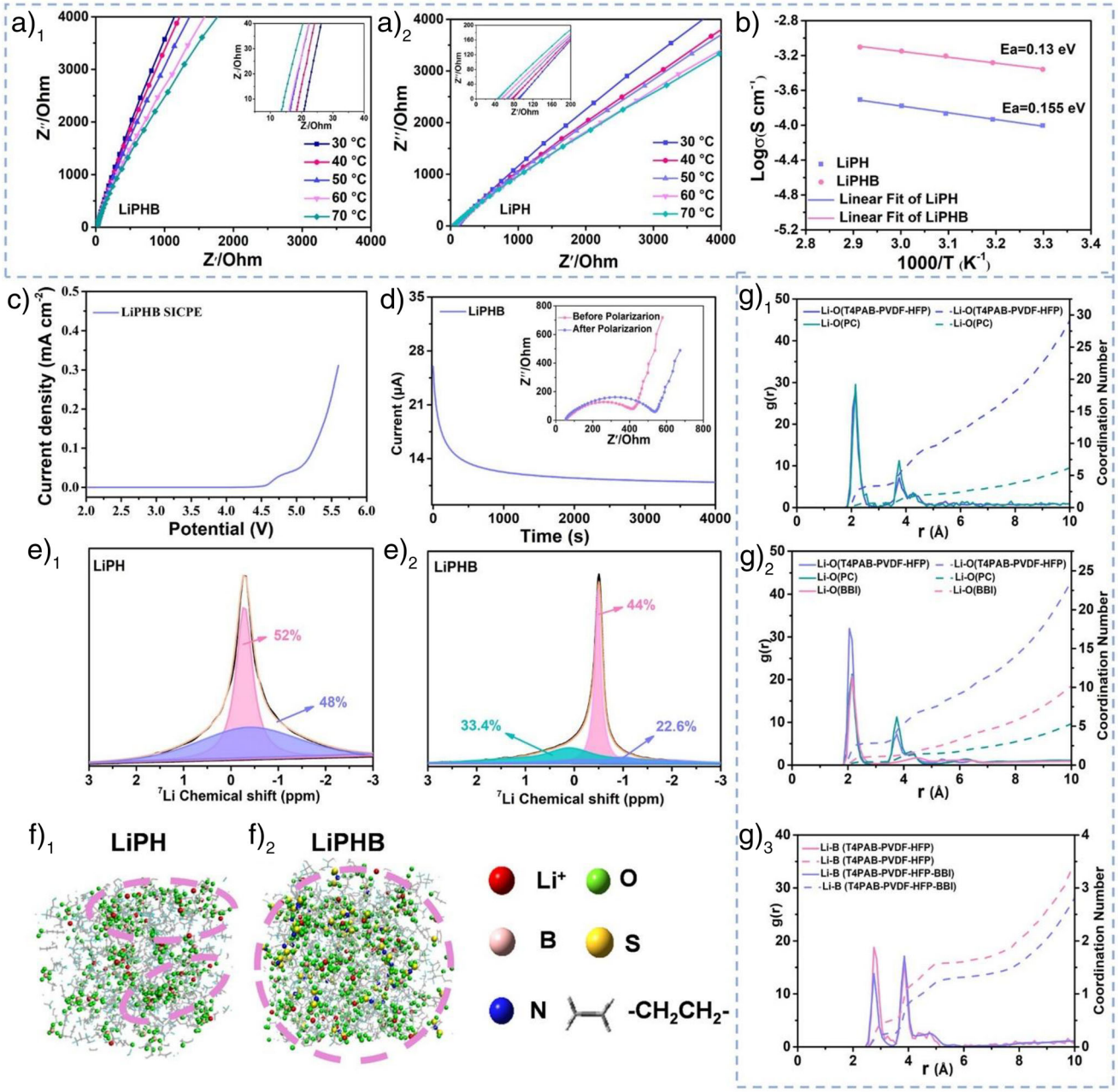

Figure 4. a) and b) EIS testing at different temperatures for LiPHB and LiPH, along with corresponding temperature-log conductivity fitting graph; c) CV testing for LiPHB; d) the dynamic impedance profiles and chronoamperometry test for calculating lithium-ion transference number. e) Solid-state nuclear magnetic resonance Li spectra of LiPH and LiPHB. f) Schematic diagram of MD molecular dynamics simulation structures of LiPH and LiPHB; g) Radial distribution function and coordination number of Li-O and Li-B in LiPH and LiPHB with PC.

lithium salt structure at the cross-linking site is highly flexible and versatile.

Electrochemical Properties and Lithium-Ion Transport

According to the electrochemical impedance spectroscopy (EIS), the lithium ion conductivity of LiPHB at 30 °C is 5.9×10^{-4} S cm^{-1} (Figure 4a$_1$), which is approximately six times higher than 9.8×10^{-5} S cm^{-1} of LiPH in Figure 4a$_2$. Furthermore, the temperature dependent conductivity between 30 and 70 °C in Figure 4b shows linear Arrhenius-type behavior, indicating that the polymer matrix is the primary environment for Li^+ transport.[13,40] And the lithium ion diffusion activation energy (E_a) of LiPHB and LiPH is calculated to be 0.133 and 0.155 eV, respectively, indicating a lower cation transport barrier in LiPHB. In addition, the LiPHB has a broader electrochemical stability window up to 4.6 V in Figure 4c against oxidation reactions.

To study the single ion conductivity characteristics of LiPHB, steady-state current measurements were carried out at 25 °C and a potential polarization of 10 mV to determine lithium ion transference number (t_{Li}^+) in Figure 4d.[4,21,41,42] The polarization curves of the initial and steady impedance spectra are shown in the inset. Specifically, the transference number is determined to be 0.7, significantly higher than that of dual-ion conductive SPEs (e.g., t_{Li}^+ = 0.23 of PVDF-HFP-TMPTA/LiTFSI prepared by in situ thermal polymerization[43]). However, the lithium-ion transference number of 0.7 falls below unity, which may be interfered with by the migration of BBI due to the weak electrostatic interaction between BBI and the polymer matrix.[44,45]

^{7}Li solid-state nuclear magnetic resonance (SSNMR) was performed to explore the chemical coordination environment of Li^+ and ion transport mechanism in the electrolytes, as shown in Figure 4e. There are two kinds of Li^+ coordination environments in LiPH (Figure 4e$_1$). The left peak at −0.29 ppm accounts for 52% of the total integral, corresponding to Li^+ coordinated with oxygen atoms in the boron ester group of LiPH. The right peak at 0.45 ppm, which accounts for 48% of the total integral, is attributed to Li^+ ions coordinated with boron atoms. With the introduction of BBI (Figure 4e$_2$), there are three Li^+ coordination environments in LiPHB. In detail, the integral area of Li^+ coordinated with oxygen atoms of the boron ester group in LiPH decreases slightly, and the integral area of Li^+ coordinated with boron atoms decreases from 48% to 22.6%, whereas the Li^+ ions coordinated with oxygen atoms in BBI at 0.14 ppm appear and account for 33.4% of the total integral.[23] Furthermore, the solid-state nuclear magnetic resonance lithium spectrum shows a significantly narrowed line width of LiPHB, indicating that the presence of BBI contributes to a further increase of the lithium ion transference freedom. Considering that a small amount of PC was introduced to wet the electrolyte-electrode interface before assembling the battery, the impact of PC on lithium-ion transport was evaluated. Molecular dynamics (MD) simulation was employed to analyze the coordination environment of lithium ions. The MD model schematic diagram (Figure 4f$_1$-f$_2$) shows that the introduction of BBI significantly reduces the agglomeration of lithium ion, forming a uniform and complete lithium ion transport network. Additionally, Figure S12 provides a static distribution of the molecular structure at the lowest energy state from the MD simulation trajectory, indicating a regular and uniform molecular distribution of the system. Figure 4g$_1$ shows the radial distribution function (RDF) and coordination number (CN) of Li—O in LiPH with PC. It can be observed that at 2.8 Å in the first solvation shell, the CN of Li—O in the boron ester group of LiPH is 3.4, while in the carboester group of PC is 0.6. This indicates that LiPH not only provides mechanical properties but also serves as the main chemical environment for Li^+ transport, with a small amount of Li^+ being transported in the form of $Li(PC)_x^+$ clusters. Figure 4g$_2$ illustrates RDF and CN of Li—O in LiPHB with PC. At 2.8 Å, CN of Li—O in the boron ester group of LiPHB is 2.8, while in the carboester group of PC is 0.4, and in the sulfonimide group of BBI is 1.1. It is evident that the oxygen atom density surrounding Li^+ in the polymer matrix is dominated in the coordination environments, indicating that the polymer matrix remains the primary environment for Li^+ transport even interfacial wetted by a small amount of PC. Additionally, the introduction of BBI provides a new Li^+ coordination environment, reducing CN of Li^+ in the polymer matrix and lowering the energy barrier for Li^+ diffusion. This suggests that the incorporation of BBI reduces the coordination strength of Li^+ in the polymer matrix, effectively aiding Li^+ ions in their transport along main chain of LiPHB. Meanwhile, Figure 4g$_3$ demonstrates that the CN of Li-B in LiPH with PC is 0.4, while that in LiPHB with PC is 0.2, which is highly consistent with SSNMR results. It is noteworthy that the introduction of BBI significantly reduces the boron atom density surrounding Li^+, further indicating that the incorporation of BBI effectively promotes the dissociation and transport of Li^+ in LiPHB.

Li Deposition Behavior

Figure 5a shows the constant current cycling test, with a current density of 0.1 mA cm^{-2} and an areal capacity of 0.05 mAh cm^{-2}. The electrolyte exhibits excellent stability in long-term cycling exceeding 1500 h, indicating its outstanding interfacial compatibility. Furthermore, the battery can still cycle for over 220 and 80 h when the current density is increased to 0.2 and 0.5 mA cm^{-2}, respectively (Figure 5b).

The critical current density (CCD) is an important parameter for determining the power density of solid-state batteries. As shown in Figure 5c, the LiPHB SICPEs can reach a stable polarization voltage plateau of 1 mA cm^{-2}, demonstrating outstanding lithium plating/stripping performance. To further validate the actual electrochemical stability of SICPEs in NCM811 batteries, the oxidation stability is evaluated by measuring the leakage current during constant voltage charging in electrochemical floating test. As shown in Figure 5d, an increase in current up to 4.6 V demonstrates a wide electrochemical stability window of LiPHB in NCM811 batteries.

SEM characterization was performed on the surface of metal lithium before cycling (Figure 5f), as well as on the lithium negative electrode after cycling at 0.2 mA cm^{-2} (Figure 5g), 0.5 mA cm^{-2} (Figure 5h), and 0.1 mA cm^{-2} for 1500 h (Figure 5i). Clearly, the lithium surface before cycling was smooth and robust. By using LiPHB solid electrolyte, no obvious lithium dendrites appear on the lithium surface even after long cycling at different current densities. To investigate the excellent compatibility between LiPHB and the lithium negative electrode, high-resolution X-ray photoelectron spectroscopy (XPS) was used to verify the composition of the solid electrolyte interface (SEI) layer on the lithium after cycling at 0.1 mA cm^{-2} (Figure 5e).[22,46,47] The presence of LiF-rich SEI (684.8 eV) is beneficial for stabilizing interface between LiPHB solid electrolyte and lithium anode.[34] All the above results corroborate that LiPHB with the fast ion transport, high lithium ion transference number, good structural flexibility, and excellent interface compatibility contributes to more uniform Li^+ flux, thereby significantly improving the uniform deposition and plating/stripping reversibility of lithium.

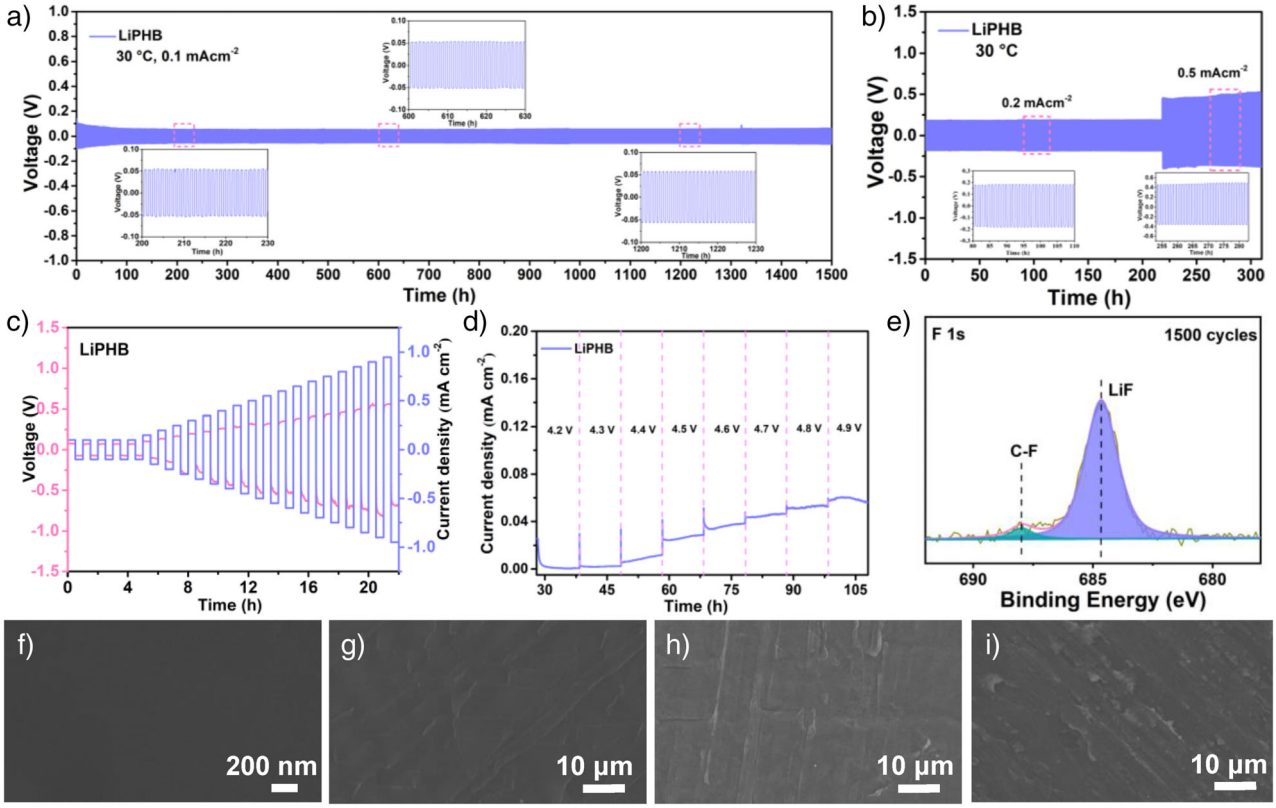

Figure 5. Lithium plating/stripping test of Li/LiPHB SICPEs/Li at a) 30 °C, 0.1 mA cm^{-2}, b) 30 °C, 0.2 mA cm^{-2}, and 0.5 mA cm^{-2}; c) the critical current density (CCD) test of LiPHB; d) electrochemical floating test of LiPHB; e) XPS test of the lithium metal negative electrode after lithium plating/stripping for 1500 h; SEM test of the lithium metal negative electrode: f) before cycling; g) cycling at 0.2 mA cm^{-2} for 200 h; h) cycling at 0.5 mA cm^{-2} for 80 h; i) after cycling for 1500 h at 0.1 mA cm^{-2}.

Li/LiPHB SICPEs/Cu cells were assembled to further evaluate the uniform Li^+ flux of SICPEs.[48,49] The reversibility of Li plating/stripping was evaluated through nucleation overpotential and average Coulombic efficiency tests (Figure S13). The results show that even under harsh conditions, the nucleation overpotential of the initial Li deposition on Cu foil is only 26.5 mV, and Li/LiPHB SICPEs/Cu cells exhibit a Coulombic efficiency of 87.1%. Moreover, the constant-current cycling curves of Li/LiPHB SICPEs/Cu reveal the uniform nucleation and growth of lithium. In contrast, the test cell using LiPH demonstrates a severe polarization (Figure S14). The results suggest that exceptional molecular structural resilience and strength of LiPHB as solid polymer electrolyte are crucial for lithium deposition behavior, effectively guiding uniform lithium deposition and inhibiting lithium dendrite growth.

Performance of Solid-State Batteries

Figure 6a–c demonstrate Li/LiPHB SICPEs/NCM811 cycling performance, with the initial discharge capacity of 140 mAh g^{-1} and Coulombic efficiency of 93.9%. It delivers a reversible capacity of 126 mAh g^{-1} with a high capacity retention rate of 90.3% in 150 cycles at 30 °C and 0.2 C. Additionally, the cycling performance in Figure S14a,b shows that Li/LiPHB SICPEs/NCM811 has a high capacity retention of 90.6% after 120 cycles at 30 °C and 0.1 C, with the initial discharge capacity of 156 mAh g^{-1} and Coulombic efficiency of 86.2%. Furthermore, Li/LiPHB SICPEs/NCM811 in Figure S15c,d has a high capacity retention of 83.5% after 140 cycles at 30 °C and 0.5 C, with the initial discharge capacity of 135 mAh g^{-1} and Coulombic efficiency of 89.8%. SEM images in Figure 6d,e show that the NCM811 particles maintain their original morphology after 150 cycles, with no structural cracking or collapse during repeated cycles as reported previously.[17,50] Notably, after the LiPHB membrane was rinsed with DMC solvent and dried, it retained its integrity and nearly returned to its original state in Figure 6f. The phenomena indicate that the LiPHB sample can withstand the volume changes caused by the repeated intercalation/deintercalation of lithium ions in the NCM811 cathode. Study the bending interface evolution of Li/LiPHB SICPEs/NCM811 cells in the electrochemical process by in situ EIS test, as shown in Figure 6g,h. Throughout the entire charge-discharge cycle, there was no significant change in the impedance, further confirming the excellent interface stability of the LiPHB membrane during cycling.[51] Furthermore, the comparison with the recently reported electrolytes in Table S1 demonstrates obviously the outstanding mechanical properties and excellent electrochemical performance of LiPHB, which verifies a tremendous potential toward practical application in solid-state batteries.

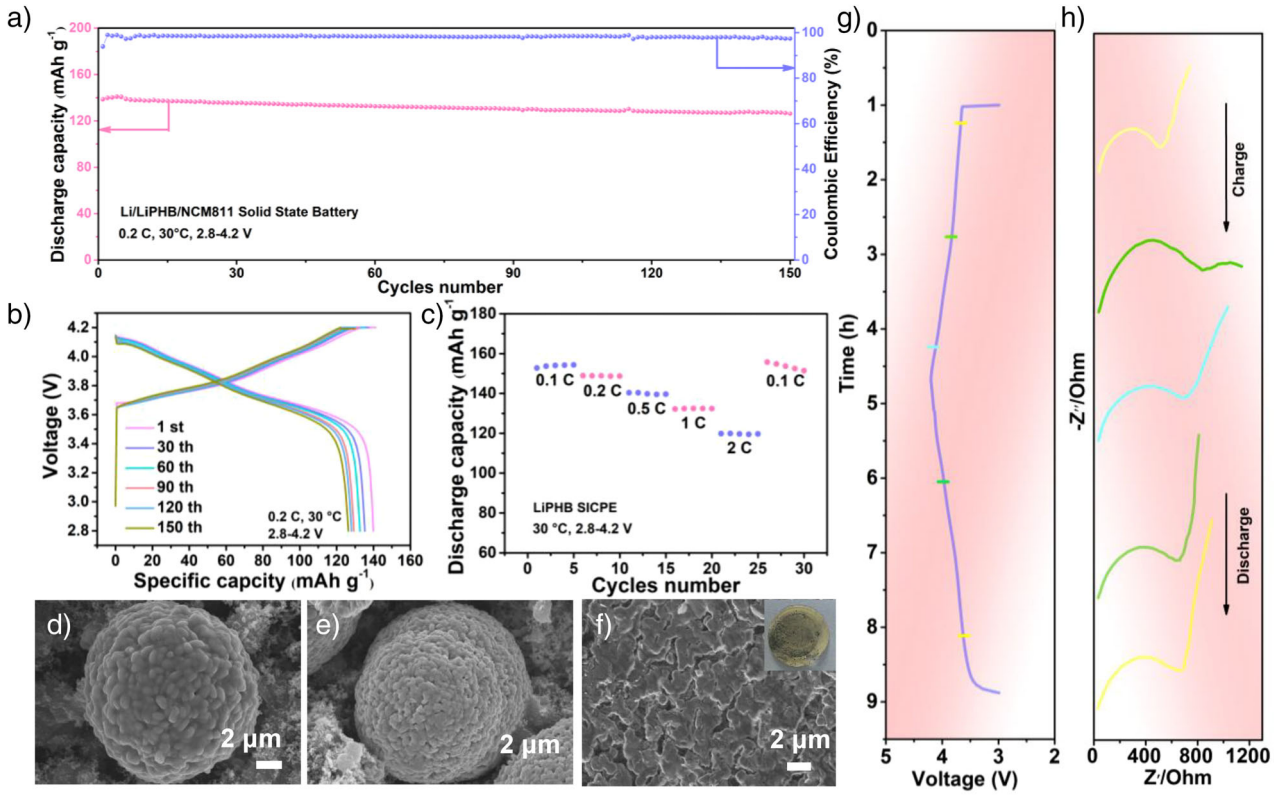

Figure 6. a) Cycling performances, b) Charge/discharge, and c) Rate capability of the Li/LiPHB SICPEs/NCM811 battery at 0.2 C and 30 °C; SEM images of the NCM811 d) before cycling and e) after cycling (inset is a photograph of the positive electrode sheet and electrolyte membrane of the cell disassembled after cycling); f) SEM image of LiPHB after cycling (inset is a photograph of the rinsed electrolyte membrane after cycling); In situ EIS data of Li/LiPHB SICPEs/NCM811 battery at different states of charge (SOC) under 30 °C, including g) voltage curve and h) the Nyquist plot.

Conclusion

In summary, an adaptive 3D-constructed LiPHB single-ion conducting polymer electrolyte was synthesized by using our designed boron ion-centered lithium salt LiT4PAB cross-linked with PVDF-HFP. The LiPHB framework with the abundant conformation not only provides mechanical strength but also deformation capability (strain of 447.4% and elasticity of 1.4 GPa), which can adapt to the volume changes during lithium plating/stripping. Moreover, LiPHB offers the homogeneous single lithium-ion transport channel to guide uniform lithium deposition. As a result, LiPHB achieves high lithium-ion conductivity of 5.9×10^{-4} S cm^{-1} at 30 °C, lithium-ion transference number of 0.7, wide electrochemical stability window of 4.6 V, and high critical current density of 1 mA cm^{-2}. Additionally, the robust-flexible skeleton of LiPHB and the LiF-rich SEI film are capable of withstanding the significant volume changes of NCM811, exhibiting excellent interface compatibility and structural integrity. Assembled lithium–lithium symmetric cells underwent galvanostatic cycling tests at 30 °C, maintaining stable cycling for over 1500 h at 0.1 mA cm^{-2}. Importantly, even under harsh conditions in the asymmetric Li//Cu cells, the nucleation overpotential of the initial Li deposition on Cu foil is only 26.5 mV, indicating the capability of LiPHB SICPEs to guide uniform lithium deposition. Furthermore, NCM811 cells deliver a discharge capacity of 126 mAh g^{-1} and high-capacity retention of 90.3% at 30 °C and 0.2 C for 150 cycles. This work provides novel structural design strategies to address the trade-off between mechanical strength and deformation capacity of solid polymer electrolyte for high-energy-density batteries.

Author Contributions

Zhaoxia Yang: Formal analysis; data curation; writing—review and editing. **Yuning Ye**: Methodology; data curation; software. **Nan Meng**: Methodology; software; supervision. **Fang Lian**: Writing—review and editing; supervision; funding acquisition; conceptualization.

Acknowledgements

This work was financially supported by the Ministry of Industry and Information Technology High-Quality Development Special Program (No. 2024-ZM02-0037).

Conflict of Interests

The authors declare no conflict of interest.

Data Availability Statement

The data that support the findings of this study are available from the corresponding author upon reasonable request.

Keywords: Dynamic cross-linked structure · Interface engineering · Mechanical Properties · Singe-ion conducting polymer electrolyte · Solid-state batteries

[1] J. B. Goodenough, A. Manthiram, *MRS Commun.* **2014**, *4*, 135–142.
[2] Q. Ma, X. X. Zeng, J. Yue, Y. X. Yin, T. T. Zuo, J. Y. Liang, Q. Deng, X. W. Wu, Y. G. Guo, *Adv. Energy Mater.* **2019**, *9*, 1803854.
[3] J. Ma, S. Zhang, Y. Zheng, T. Huang, F. Sun, S. Dong, G. Cui, *Adv. Mater.* **2023**, *35*, e2301892.
[4] N. Meng, Y. Ye, Z. Yang, H. Li, F. Lian, *Adv. Funct. Mater.* **2023**, *33*, 2214881.
[5] Y. Feng, Y. Fan, L. Zhao, J. Yu, Y. Liao, T. Zhang, R. Zhang, H. Zhu, X. Sun, Z. Hu, K. Zhang, J. Chen, *Angew. Chem. Int. Ed.* **2025**, *64*, e202417105.
[6] J. Chazalviel, *Phys. Rev. A* **1990**, *42*, 7355–7367.
[7] D. J. Bannister, G. R. Davies, I. M. Ward, J. E. Mclntyre, *Polymer* **1984**, *25*, 1291.
[8] K. Jeong, S. Park, S.-Y. Lee, *J. Mater. Chem. A* **2019**, *7*, 1917–1935.
[9] S. Z. Zhang, X. H. Xia, D. Xie, R. C. Xu, Y. J. Xu, Y. Xia, J. B. Wu, Z. J. Yao, X. L. Wang, J. P. Tu, *J. Power Sources* **2019**, *409*, 31–37.
[10] W. Zhang, V. Koverga, S. Liu, J. Zhou, J. Wang, P. Bai, S. Tan, N. K. Dandu, Z. Wang, F. Chen, J. Xia, H. Wan, X. Zhang, H. Yang, B. L. Lucht, A.-M. Li, X.-Q. Yang, E. Hu, S. R. Raghavan, A. T. Ngo, C. Wang, *Nat. Energy.* **2024**, *9*, 386–400.
[11] T. H. Naren, Q. Gu, R. Jiang, Y. Zhao, L. Zhang, A. Zhu, X. H. Wang, J. H. Wu, Z. H. Zheng, C.-S. H. Lee, G.-C. Kuang, L. Chen, F.-R. H. Chen, Q. Zhang, *Angew. Chem. Int. Ed.* **2025**, e202509921.
[12] J. Gou, K. Cui, S. Wang, Z. Zhang, J. Huang, H. Wang, *Nat. Commun.* **2025**, *16*, 3626.
[13] W. Liu, C. Yi, L. Li, S. Liu, Q. Gui, D. Ba, Y. Li, D. Peng, J. Liu, *Angew. Chem. Int. Ed.* **2021**, *60*, 12931–12940.
[14] Z. Yu, D. G. Mackanic, W. Michaels, M. Lee, A. Pei, D. Feng, Q. Zhang, Y. Tsao, C. V. Amanchukwu, X. Yan, H. Wang, S. Chen, K. Liu, J. Kang, J. Qin, Y. Cui, Z. Bao, *Joule.* **2019**, *3*, 2761–2776.
[15] K. Jeong, S. Park, G. Jung, S. Kim, Y.-H. Lee, S. Kwak, S.-Y. Lee, *J. Am. Chem. Soc.* **2019**, *141*, 5880–5885.
[16] J. Sun, H. Yuan, J. Yang, T. Wang, Y. Gao, Q. Zhao, X. Liu, H. Wang, Y. W. Zhang, J. Wang, *InfoMat.* **2023**, *6*, e12487.
[17] L. Lin, K. Qin, Q. Zhang, L. Gu, L. Suo, Y. s. Hu, H. Li, X. Huang, L. Chen, *Angew. Chem. Int. Ed.* **2021**, *60*, 8289–8296.
[18] J. Zhu, Z. Zhang, S. Zhao, A. S. Westover, I. Belharouak, P. F. Cao, *Adv. Energy Mater.* **2021**, *11*, 2003836.
[19] W. Zhou, Z. Wang, Y. Pu, Y. Li, S. Xin, X. Li, J. Chen, J. B. Goodenough, *Adv. Mater.* **2019**, *31*, e1805574.
[20] K. Dai, Y. Zheng, W. Wei, *Adv. Funct. Mater.* **2021**, *31*, 2008632.
[21] H. Zhang, C. Li, M. Piszcz, E. Coya, T. Rojo, L. M. Rodriguez-Martinez, M. Armand, Z. Zhou, *Chem. Soc. Rev.* **2017**, *46*, 797–815.
[22] K. Liu, A. Pei, H. R. Lee, B. Kong, N. Liu, D. Lin, Y. Liu, C. Liu, P.-c. Hsu, Z. Bao, Y. Cui, *J. Am. Chem. Soc.* **2017**, *139*, 4815–4820.
[23] Y. Ye, X. Zhu, N. Meng, F. Lian, *Adv. Funct. Mater.* **2023**, *33*, 2307045.
[24] J. Zhao, M. Hong, Z. Ju, X. Yan, Y. Gai, Z. Liang, *Angew. Chem. Int. Ed.* **2022**, *61*, e202214386.
[25] X. Miao, S. Guan, C. Ma, L. Li, C.-W. Nan, *Adv. Mater.* **2023**, *35*, e2206402.
[26] H. Adenusi, G. A. Chass, S. Passerini, K. V. Tian, G. Chen, *Adv. Energy Mater.* **2023**, *13*, 2203307.
[27] D. M. Shin, J. E. Bachman, M. K. Taylor, J. Kamcev, J. G. Park, M. E. Ziebel, E. Velasquez, N. N. Jarenwattananon, G. K. Sethi, Y. Cui, J. R. Long, *Adv. Mater.* **2020**, *32*, e1905771.
[28] Y. Du, H. Yang, J. M. Whiteley, S. Wan, Y. Jin, S. H. Lee, W. Zhang, *Angew. Chem. Int. Ed.* **2016**, *55*, 1737–1741.
[29] H.-D. Nguyen, G.-T. Kim, J. Shi, E. Paillard, P. Judeinstein, S. Lyonnard, D. Bresser, C. Iojoiu, *Energy Environ. Sci.* **2018**, *11*, 3298–3309.
[30] T. Zhou, Y. Zhao, J. W. Choi, A. Coskun, *Angew. Chem. Int. Ed.* **2021**, *60*, 22791–22796.
[31] X. Shen, H. M. Hua, H. Li, R. Y. Li, T. X. Hu, D. Z. Wu, P. Zhang, J. B. Zhao, *Polymer* **2020**, *201*, 122568.
[32] C. Zhang, H. Zheng, L. Lin, J. Wen, S. Zhang, X. Hu, D. Zhou, B. Sa, L. Wang, J. Lin, Q. Xie, D. L. Peng, J. Lu, *Adv. Energy Mater.* **2024**, *14*, 2402068.
[33] G. Jiang, J. Liu, J. He, H. Wang, S. Qi, J. Huang, D. Wu, J. Ma, *Adv. Funct. Mater.* **2023**, *33*, 2214422.
[34] X. Zeng, L. Dong, J. Fu, L. Chen, J. Zhou, P. Zong, G. Liu, L. Shi, *Chem. Eng. J.* **2022**, *428*, 131100.
[35] B. Tong, Z. Song, W. Feng, J. Zhu, H. Yu, X. Huang, M. Armand, Z. Zhou, H. Zhang, *Adv. Energy Mater.* **2023**, *13*, 2204085.
[36] K. S. Oh, J. H. Kim, S. H. Kim, D. Oh, S. P. Han, K. Jung, Z. Wang, L. Shi, Y. Su, T. Yim, S. Yuan, S. Y. Lee, *Adv. Energy Mater.* **2021**, *11*, 210181.
[37] H. Li, Y. Du, Q. Zhang, Y. Zhao, F. Lian, *Adv. Energy Mater.* **2022**, *12*, 2103530.
[38] T. Lu, Q. Chen, *Chem.-Methods* **2021**, *1*, 231–239.
[39] L. Meabe, S. R. Peña, M. Martinez-Ibañez, Y. Zhang, E. Lobato, H. Manzano, M. Armand, J. Carrasco, H. Zhang, *J. Phys. Chem. C* **2020**, *124*, 17981–17991.
[40] N. Meng, F. Lian, G. Cui, *Small* **2020**, *17*, 2005762.
[41] J. Gao, C. Wang, D.-W. Han, D.-M. Shin, *Chem. Sci.* **2021**, *12*, 13248–13272.
[42] P. Zhou, X. Zhang, Y. Xiang, K. Liu, *Nano Res.* **2023**, *16*, 8055–8071.
[43] Y. Hu, L. Li, H. Tu, X. Yi, J. Wang, J. Xu, W. Gong, H. Lin, X. Wu, M. Liu, *Adv. Funct. Mater.* **2022**, *32*, 2203336.
[44] C. Lei, T. Zhou, M. Zhang, T. Liu, C. Xu, R. Wang, X. He, X. Liang, *Adv. Sci.* **2024**, *11*, 2405482.
[45] X. He, Y. Ni, Y. Hou, Y. Lu, S. Jin, H. Li, Z. Yan, K. Zhang, J. Chen, *Angew. Chem. Int. Ed.* **2021**, *60*, 22672–22677.
[46] Y. Wang, Y. Sun, D. Zhang, M. Pan, Y. Chen, S. Chen, S. Zhang, Y. Zhao, J. Wang, Y. NuLi, *Energy Storage Mater.* **2024**, *65*, 103152.
[47] R. Xu, Y. Xiao, R. Zhang, X.-B. Cheng, C.-Z. Zhao, X.-Q. Zhang, C. Yan, Q. Zhang, J.-Q. Huang, *Adv. Mater.* **2019**, *31*, e1808392.
[48] B. D. Adams, J. Zheng, X. Ren, W. Xu, J. G. Zhang, *Adv. Energy Mater.* **2017**, *8*, 1702097.
[49] C. Heubner, S. Maletti, H. Auer, J. Hüttl, K. Voigt, O. Lohrberg, K. Nikolowski, M. Partsch, A. Michaelis, *Adv. Funct. Mater.* **2021**, *31*, 51.
[50] P. Albertus, S. Babinec, S. Litzelman, A. Newman, *Nat. Energy* **2017**, *3*, 16–21.
[51] L. Zhao, Y. Du, C. Wang, D. Li, H. Li, Y. Zhao, *Energy Storage Mater.* **2024**, *68*, 103360.

Manuscript received: March 05, 2025
Revised manuscript received: June 24, 2025
Accepted manuscript online: July 20, 2025
Version of record online: ■■, ■■